Check for updates

Superhydrophilicity of photocatalytic ZnO/SnO$_2$ heterostructure for self-cleaning applications

Talinungsang[1] · Diliraj Upadhaya[1] · Pankaj Kumar[1] · Debarun Dhar Purkayastha[1]

Abstract

Sol–gel spin coating technique was used to deposit thin films of ZnO, SnO$_2$, and ZnO/SnO$_2$ on a borosilicate glass substrate. The films were characterized using XRD, FESEM, EDX, HRTEM, AFM, UV-Vis spectrophotometer, and contact angle meter. X-ray diffraction confirms the presence of both hexagonal wurtzite and tetragonal phase of ZnO and SnO$_2$ respectively in ZnO/SnO$_2$. Wettability studies reveal that ZnO/SnO$_2$ film is superhydrophilic with water contact angle of 3.4°. The photocatalytic performance of the films is evaluated by measuring the degradation of an aqueous solution of methylene blue, methyl orange, and their mixture. The degradation of stearic acid adsorbed on the film's surface is measured by tracking the water contact angle after UV irradiation as a function of time. The excellent photocatalytic activity of ZnO/SnO$_2$ thin films is attributed to formation of type-II heterostructure between ZnO and SnO$_2$, which inhibits the charge recombination between photogenerated electrons and holes. The ZnO/SnO$_2$ shows good photocatalytic activity after five recycling runs. ZnO/SnO$_2$ thin films being excellent photocatalyst along with its superhydrophilic nature will have potential application in self-cleaning and antifogging.

Graphical Abstract
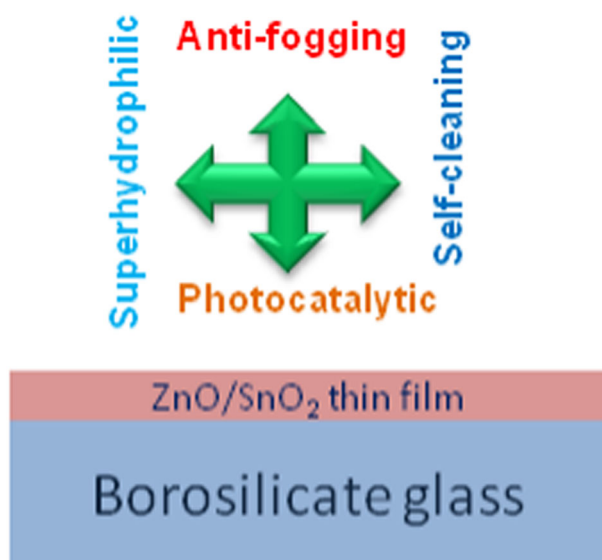
✉ Debarun Dhar Purkayastha
ddebarun@yahoo.com

1 Department of Physics, National Institute of Technology
Nagaland, Chumukedima 797103, India

Highlights

- SnO$_2$, ZnO and ZnO/SnO$_2$ thin films were prepared by a cost-effective sol-gel method.
- ZnO/SnO$_2$ thin films show superhydrophilic character.
- Degradation of pollutants in solid and liquid phase was evaluated.
- ZnO/SnO$_2$ shows superior photocatalytic activity due to heterostructure formation.

1 Introduction

Superhydrophilic surfaces (SHS) with water contact angle (WCA) less than 5° have been a center of attention in research and industries mainly due to their applications in self-cleaning and antifogging effects [1–3]. Generally, the wettability of a surface is influenced by its surface energy and roughness. Hence, SHS can be accomplished by maneuvering the chemical composition and morphology of the surface [4–6]. It is a well-known fact that SHS has high surface energy. This makes them susceptible to adhesion of contaminants, which deplete the superhydrophilic nature of the surface. Therefore, it is desirable to have SHS, which can photocatalytically degrade contaminants by natural means. There are reports of achieving superhydrophilicity of metal oxide semiconductors (TiO$_2$, ZnO) by the generation of surface oxygen vacancies upon photoirradiation [7–9]. The hydroxyl group of atmospheric water adsorbed over the surface oxygen vacancies present in the photocatalyst leads to the formation of SHS [10]. It must be noted that hydroxyl groups on the surface stimulate the photocatalytic activity of metal oxides by chemical degradation of organic pollutants. In this way, the photocatalyst involves in breaking down the pollutant from the surface, whereas the superhydrophilic character causes the water to stretch over it, which carries away the filth and impurities.

TiO$_2$ has been widely studied because of its photocatalytic activity [2]. Among the metal oxides, ZnO is a suitable alternative to TiO$_2$ because its photodegradation mechanism is similar to that of TiO$_2$ and ZnO has approximate equal band gap energy like TiO$_2$. However the photocatalytic efficiency of single-phase ZnO or TiO$_2$ semiconductor is significantly low because of the quick recombination between photogenerated electrons and holes. ZnO ($E_g = 3.37$ eV) and SnO$_2$ ($E_g = 3.6$ eV) are wide band gap, n-type semiconductor, which are studied for their widespread application in antimicrobial, sensors, photocatalyst, and self-cleaning surfaces [11–16]. Their photocatalytic property is particularly studied because on coupling them together their efficiency gets increased considerably as compared with individual form [17–21]. This is mainly due to the formation of heterostructure that inhibits charge recombination of electron and holes. Although there are many published reports of ZnO/SnO$_2$ heterostructures

for degradation of organic pollutants in powder form, depositing it in the form of films gives the added benefit to it by being solid and can be recycled easily [22–25]. Recently, we have demonstrated the significant improvement in wettability and photocatalytic efficiency of ZnO/SnO$_2$ thin films with annealing temperature [26]. But charge ion diffusion from the substrate during annealing may alter the properties of films [27]. So in order to prevent that we have prepared the bilayer ZnO/SnO$_2$ heterostructure and comparative study was made with monolayer component. The wettability studies reveal that ZnO/SnO$_2$ thin films exhibit superhydrophilic character with a very high degree of transparency. The photocatalytic activity of the films was assessed by measuring the degradation of an aqueous solution of methylene blue (MB), methyl orange (MO), and their mixture. Apart from degradation of dyes in aqueous form, degradation of a thin layer of stearic acid adsorbed on the film surface was also assessed by measuring the change in WCA as a function of photoirradiation time. The transparent superhydrophilic ZnO/SnO$_2$ films being photocatalytically active will have potential application in antifogging and self-cleaning.

2 Experimental

Borosilicate glass was used as a substrate to prepare nanocrystalline films of SnO$_2$, ZnO, and ZnO/SnO$_2$ (ZnO on top and SnO$_2$ at the bottom) using sol–gel method. SnO$_2$ sol was prepared by dissolving SnCl$_2$·2H$_2$O in ethanol [15]. After stirring for 1 h at 70 °C, polyethylene glycol was added to the solution and was stirred continuously for 2 h at the same temperature to obtain a clear sol. ZnO sol was prepared by the method described elsewhere [28]. Sols of SnO$_2$ and ZnO were spin coated on BSG and annealed at 500 °C to obtain SnO$_2$ and ZnO thin films. In case of ZnO/SnO$_2$ thin films, SnO$_2$ sol is first spin coated on BSG and annealed at 500 °C followed by deposition of ZnO sol and subsequent heating at 500 °C.

A UV-Vis (Agilent Cary 60) spectrophotometer scanning over the wavelength range of 200–800 nm was used to investigate the optical properties and photocatalytic activity of the synthesized films. Contact angle meter (DMs-401, Kyowa Interface Science Co Ltd, Japan) via sessile drop

method was used to examine the wetting properties. The Owens and Wendt geometric mean two liquid method was used to calculate surface energies of thin films. An X-ray diffractometer (Rigaku Ultima IV) with Cu Kα radiation of wavelength 0.15405 nm in the 2θ range of 20°–80° was used for phase and crystal structure analysis. Field Emission Gun Scanning Electron Microscope (FEG-SEM, JSM-7600F) joint with energy dispersive X-ray (EDX) was used to determine the surface morphology and elemental composition of the films. The high-resolution transmission electron microscope (HRTEM) images were acquired by a Tecnai 20 G2 STwin, FEI electron microscope, operated at 200 kV. Atomic force microscope (AFMNT-MDT NTEGRA Vita) was used for investigating the surface roughness of the films. Nanoindentation technique (Agilent technologies, model: G 2000) was used to examine the nanomechanical properties with maximum load of 500 mN.

3 Results and discussion

The X-ray diffraction (XRD) pattern of SnO_2, ZnO, and ZnO/SnO_2 is presented in Fig. 1. It is evident from XRD pattern that SnO_2 films over BSG crystallized into the tetragonal structure (JCPDS 88-0287), whereas ZnO films show hexagonal wurtzite structure (JCPDS 89-1397). The presence of SnO_2 and ZnO crystal phase in ZnO/SnO_2 thin films is evident from the coexistence of both hexagonal wurtzite ZnO and tetragonal SnO_2. Scherrer's formula was used to calculate the average crystallite size from full-width half maxima. It can be seen that the diffraction peaks of SnO_2 are fairly broad, which gives a small average crystallite

size of 5 nm. ZnO exhibits sharp diffraction peaks, which result an increase in average crystallite size of 16.8 nm. However, in ZnO/SnO_2, the average crystallite size of ZnO reduces to 14.3 nm, which is smaller than that of pure ZnO. In contrast, the average crystallite of SnO_2 was found to be 5.1 nm, which is similar to that of pure SnO_2. This indicates that SnO_2 hamper the growth of ZnO nanocrystal in ZnO/SnO_2 [24].

The surface morphology of SnO_2, ZnO, and ZnO/SnO_2 thin films are shown in Fig. 2a–c. The particles are uniformly distributed. The measured mean particle sizes were found to be 7.68, 21.9, and 16.5 nm for SnO_2, ZnO, and ZnO/SnO_2 thin films, respectively. The thickness of the
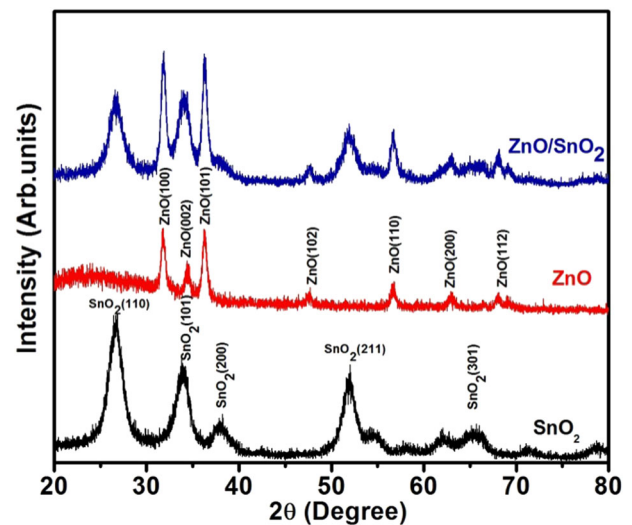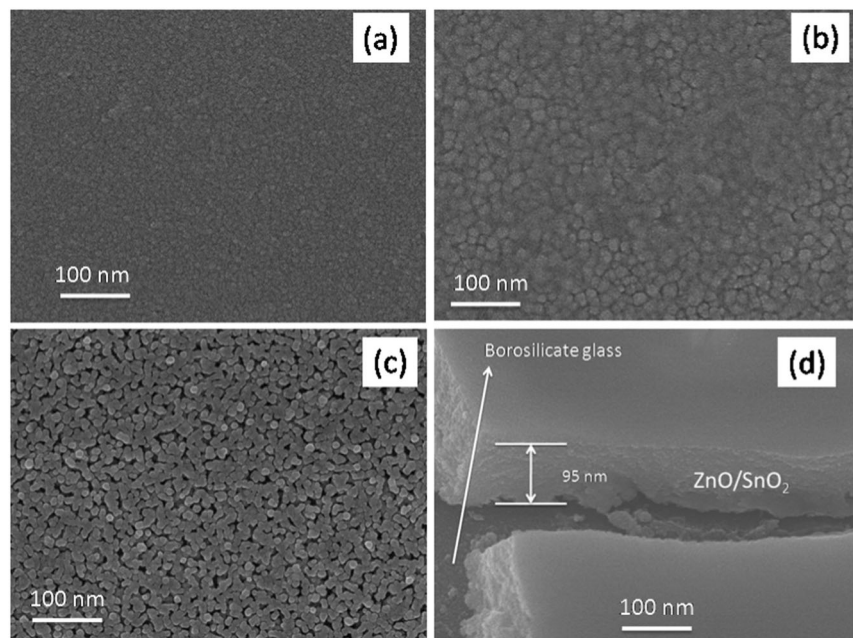

Fig. 1 X-ray diffraction pattern of SnO_2, ZnO, and ZnO/SnO_2 thin films

Fig. 2 FESEM images of **a** SnO_2, **b** ZnO, **c** ZnO/SnO_2, and **d** cross-sectional image of ZnO/SnO_2 thin films

ZnO/SnO$_2$ thin films calculated from cross-sectional FESEM image was found to be in the range of 95 nm as depicted in Fig. 2d. The EDX spectra of SnO$_2$, ZnO, and ZnO/SnO$_2$ thin films are shown in Fig. 3a–c. The existence of preferred elements in SnO$_2$, ZnO, and ZnO/SnO$_2$ films respectively are confirmed by EDX analysis. The appearances of peaks of silicon, calcium, and sodium are due to the borosilicate glass substrate. Moreover, the peaks of carbon and gold are detected due to the use of carbon tape on the stub and gold coating on the sample.

The formation of ZnO/SnO$_2$ heterostructure is further probed through HRTEM. The high crystallinity of the heterostructure is confirmed through the appearance of clear lattice fringes in the HRTEM image as shown in Fig. 4. A region having coexistence of crystalline ZnO and SnO$_2$ nanocrystals are accessed with a combination of FFT-IFFT
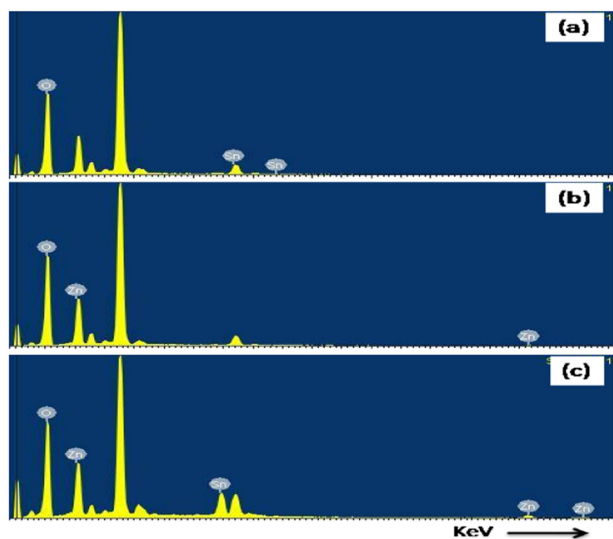

Fig. 3 EDX spectra of **a** SnO$_2$, **b** ZnO, and **c** ZnO/SnO$_2$ thin films

technique and shown as insets in Fig. 4. The two distinct lattice fringes are observed. The observed fringes correspond to interplaner distances of 3.40 Å and 2.46 Å. The calculated lattice spacing is in agreement with (110) and (101) of the tetragonal SnO$_2$ and hexagonal ZnO respectively indicating the formation of ZnO/SnO$_2$ heterostructure.

For investigating the surface wettability of SnO$_2$, ZnO, and ZnO/SnO$_2$ thin films, WCA was measured by keeping the drop volume of water as 2 µl. The variation of WCA with r.m.s roughness is shown in Fig. 5. The WCA of as-deposited SnO$_2$ and ZnO thin films is 11.8° and 83.9°. It is interesting to see that ZnO/SnO$_2$ thin films exhibit superhydrophilic character with WCA of 3.4°. The 3D AFM images of SnO$_2$, ZnO, and ZnO/SnO$_2$ thin films are shown in Fig. 6a–c. The r.m.s roughness of SnO$_2$, ZnO, and ZnO/SnO$_2$ films were found to be 46.90 nm, 11.40 nm, and 60.04 nm, respectively. It is evident from Fig. 5 that with an increase in roughness of the film, the WCA decreases, which in agreement with the Wenzel model of wetting [29].

The antifogging performance was evaluated by immersing the samples in cold water for 10 min. The samples were then placed onto a paper to examine the accumulation of mist and tiny drops of water. Due to the contrast in temperature between the cold water and the surrounding, water molecules get condensed forming a fog like layer. The optical comparison was recorded using contact angle meter and mobile lens camera. The pictorial images of glass and superhydrophilic ZnO/SnO$_2$ is shown Fig. 7a, b. Tiny droplets of water (fogging) formed on the untreated glass can be seen from Fig. 7a, whereas superhydrophilic ZnO/SnO$_2$ shows antifogging behavior. The inset of Fig. 7a, b shows that the optical transparency of bare glass is significantly reduced due to the formation of fog. However, for superhydrophilic ZnO/SnO$_2$ with
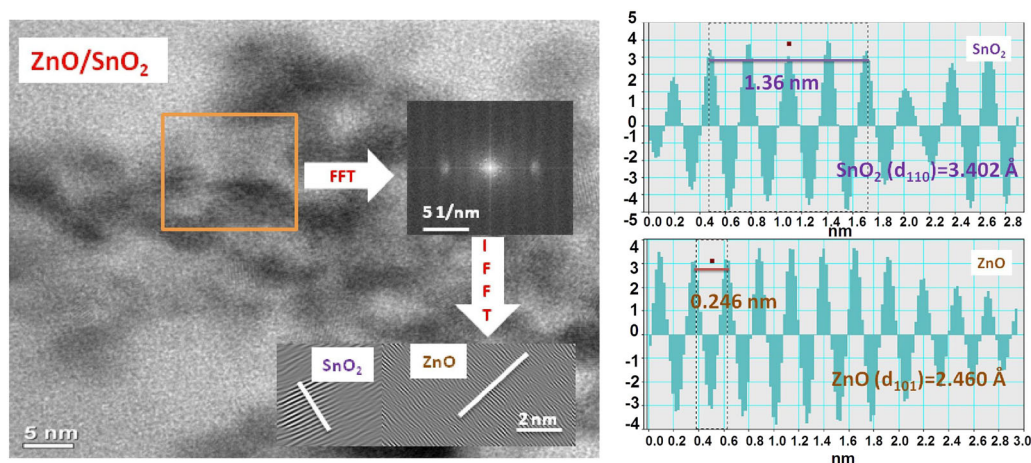

Fig. 4 High-resolution transmission electron microscope image of ZnO/SnO$_2$ heterostructure. Top and bottom inset shows FFT and IFFT image of selected region. The lattice fringe region of both the crystals line profile with computed length scale is shown in right

WCA < 5°, the water droplets on the surface will quickly spreads away, which inhibits the formation of fog. Figure 7c depicts the transmittance spectra of the films. The films were fairly transparent with ZnO and ZnO/SnO$_2$ showing transparency of more than 85% in the visible region. Superhydrophilic ZnO/SnO$_2$ films with high degree of transparency will have potential application in self-cleaning and antifogging [30].
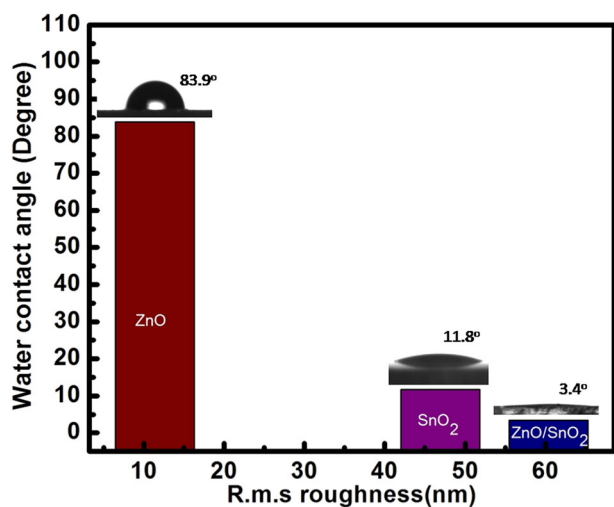
One of the major challenges for wide use of SHS with antifogging behavior is the lack of mechanical stability. Hence to probe the mechanical property (Hardness and Young's modulus) of superhydrophilic ZnO/SnO$_2$ film, nanoindentation technique was employed. The films are substantially hard with average hardness and Young's modulus are 53.8 ± 5.9 and 3.31 ± 0.47 GPa, respectively.

The adsorption of airborne organic contaminants has an adverse effect on the superhydrophilic character [31]. In order to investigate the role of organic pollutants on the superhydrophilic character of the film surface, a thin layer of stearic acid was coated on the surface of the photocatalyst. The formation of a stearic acid layer on the film surface is confirmed by FT-IR as shown in Fig. 8. The peaks at 2915 cm^{-1} and 2848 cm^{-1} correspond to –CH$_3$ asymmetrical and –CH$_2$ symmetrical stretching vibrations of stearic acid. The peaks at 1697 cm^{-1} correspond to the carboxyl group of stearic acid. Metal oxides on modification with stearic acid form a metal stearate bond with the carboxyl group attached to the metal and the alkyl group orients outward forming a self-assembled layer [32]. The surface energy of the films was measured by using Owen–Wendt geometric mean method [33]. The surface energy and WCA of films modified with stearic acid are shown in Fig. 9. The WCA of stearic acid modified SnO$_2$ and ZnO thin films are 125.6° and 108.2°, whereas stearic acid modified ZnO/SnO$_2$ thin films have WCA of 132.2°.
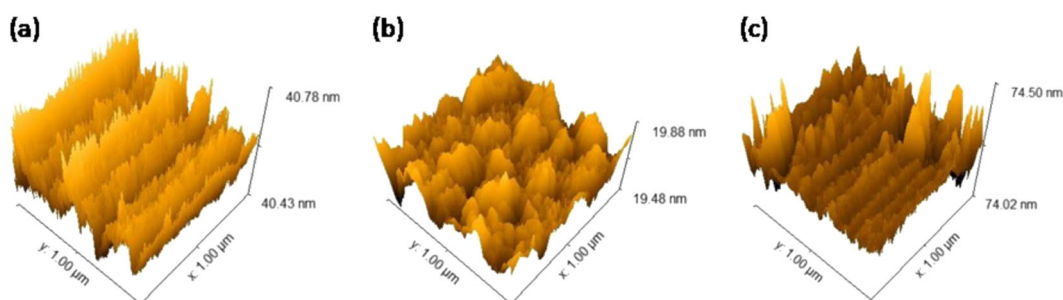

Fig. 5 Variation of the water contact angle with r.m.s roughness

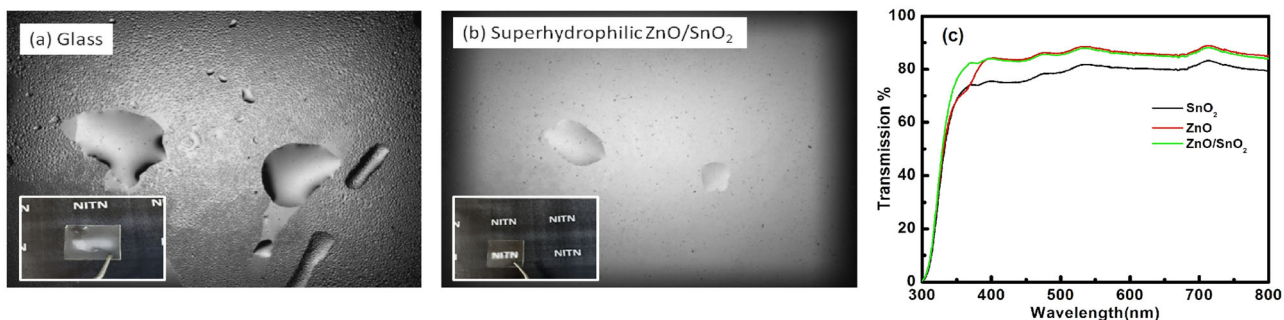Fig. 6 3D AFM images of **a** SnO$_2$, **b** ZnO, and **c** ZnO/SnO$_2$ thin films

Fig. 7 Photographic images showing the antifogging effect on **a** glass and **b** superhydrophilic ZnO/SnO$_2$ films (insets **a** and **b** show the transparency of glass and superhydrophilic ZnO/SnO$_2$ films) and **c** transmission spectra of SnO$_2$, ZnO, and ZnO/SnO$_2$ thin films
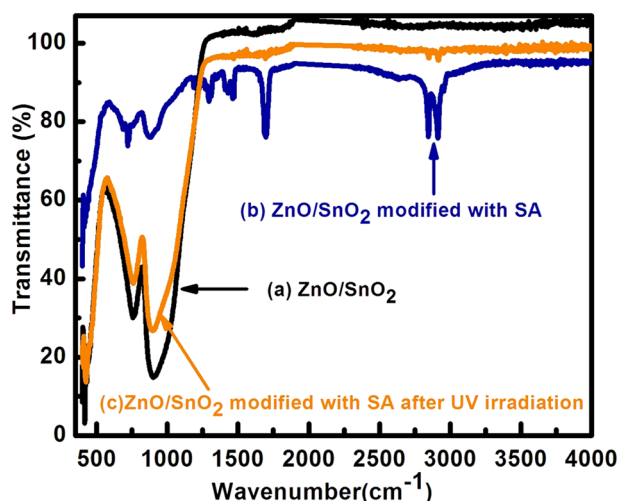
Fig. 8 FT-IR spectra of **a** ZnO/SnO$_2$, **b** ZnO/SnO$_2$ modified with stearic acid, and **c** ZnO/SnO$_2$ modified with stearic acid after UV irradiation
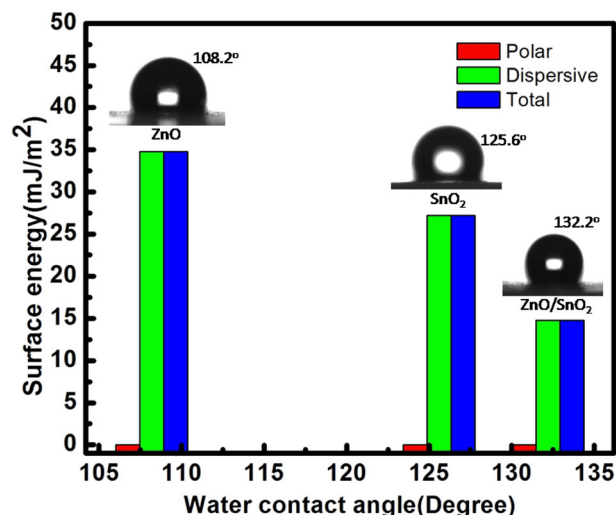

Fig. 9 Water contact angle and surface energy of stearic acid modified SnO$_2$, ZnO, and ZnO/SnO$_2$ thin films

Table 1 Surface energy of stearic acid modified SnO$_2$, ZnO, and ZnO/SnO$_2$ thin films

Sample	Polar	Surface energy (mJ/m^2)	
		Dispersive	Total
SnO$_2$ stearic acid	0	27.2	27.2
ZnO stearic acid	0	34.8	34.8
ZnO/SnO$_2$ stearic acid	0	14.8	14.8

The surface energy of stearic acid modified films is shown in Table 1. The surface energy of stearic acid modified SnO$_2$ and ZnO thin films is 27.2 and 34.8 mJ/m^2, whereas the surface energy of stearic acid modified ZnO/SnO$_2$ thin films is 14.8 mJ/m^2. It is clear from Table 1 that upon

modification with stearic acid, the polar component (water-loving) has no contribution in the total surface energy. As a result, the hydrophobicity of films is entirely due to the contribution of the dispersive component (nonpolar) in total surface energy [15].

A self-cleaning photocatalyst can only be realized if the organic pollutants are degraded from the surface of the films by natural means. The degradation of stearic acid from the surface of the films was carried out by irradiating the stearic modified films with UV light. The degradation of stearic acid is confirmed by FT-IR (Fig. 8) with the decrease in intensity of stearic acid peaks. The variation of WCA upon UV irradiation is shown in Fig. 10a. It is seen that the hydrophobic stearic modified films become hydrophilic after exposure to UV light for 60 min. To understand the rate of degradation of stearic acid, hydrophilic conversion rates were calculated from the slope of the inverse of WCA plotted against UV irradiation time (Fig. 10b). Table 2 shows the hydrophilic conversion rate of SnO$_2$, ZnO, and ZnO/SnO$_2$ thin films. The hydrophilic conversion rate was found to be $6.85 \times 10^{-4} \deg^{-1} \min^{-1}$, $5.90 \times 10^{-4} \deg^{-1} \min^{-1}$, and $12.70 \times 10^{-4} \deg^{-1} \min^{-1}$ for SnO$_2$, ZnO, and ZnO/SnO$_2$ thin films.

The photocatalytic activities of the films were further carried out by the degradation of cationic (MB), anionic (MO) dye. and their mixture (MO–MB) under UV light (254 nm, Philips Hg germicidal lamp) for 3 h. The absorbance spectra of MB, MO, and MO–MB as a function of irradiation time are shown in Fig. 11. The photocatalytic efficiency of the films was calculated by using the following equation:

$$\eta = \left(\frac{C_o - C}{C_o}\right) \times 100, \qquad (1)$$

where C_o is the initial concentration of the dye and C is the concentration after UV-irradiation time.

The photocatalytic efficiency of SnO$_2$, ZnO, and ZnO/SnO$_2$ thin films is shown in Fig. 12a–c. As inscribed in Fig. 12, SnO$_2$ degrades 85% of MB and 37% of MO, whereas ZnO degrades 59% and 34% of initial MB and MO concentration, respectively. The degradation efficiency of SnO$_2$ is higher than ZnO, which is in agreement with the earlier report [23]. The efficiency is highest for ZnO/SnO$_2$, which degrades 95% of MB and 51% of MO. To understand the rate at which the degradation was taking place, rate constant was calculated using the following pseudo first-order equation:

$$\ln\left(\frac{C_o}{C}\right) = -kt. \qquad (2)$$

The kinetics of photodegradation of MB and MO by SnO$_2$, ZnO, and ZnO/SnO$_2$ thin films are shown in Fig. 13a, b. The slope of $\ln(C_o/C)$ as a function of UV-irradiation time gives

Fig. 10 Variation of **a** water contact angle and **b** inverse of water contact angle of SnO$_2$, ZnO, and ZnO/SnO$_2$ thin films modified with stearic acid under UV light
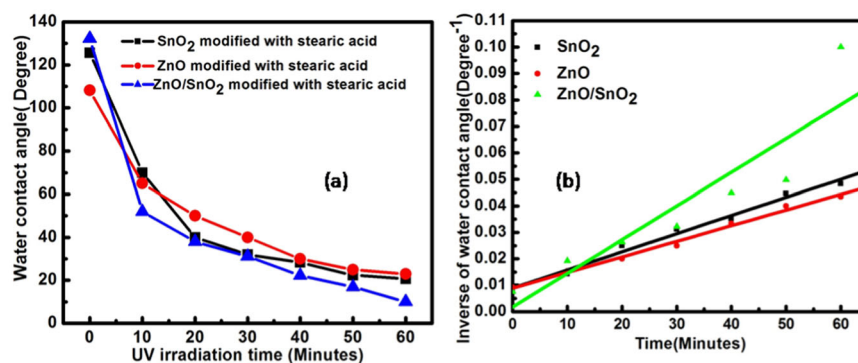

Table 2 Hydrophilic conversion rate, rate constant, and photocatalytic efficiency of SnO$_2$, ZnO, and ZnO/SnO$_2$ thin films

Samples	Hydrophilic rate constant (deg^{-1} min^{-1})	Rate constant (k) MB (min^{-1})	Rate constant (k) MO (min^{-1})	Photocatalytic efficiency (%)	
				MB	MO
SnO$_2$	6.85×10^{-4}	5.0×10^{-3}	1.12×10^{-3}	85	37
ZnO	5.90×10^{-4}	2.26×10^{-3}	1.05×10^{-3}	59	34
ZnO/SnO$_2$	12.70×10^{-4}	7.36×10^{-3}	1.81×10^{-3}	95	51

the rate constant. The rate constant of SnO$_2$, ZnO, and ZnO/SnO$_2$ thin films using MB and MO as model organic pollutants is shown in Table 2. The degradation rate of MB and MO for SnO$_2$ was found to be 5.0×10^{-3} min^{-1} and 1.12×10^{-3} min^{-1}, whereas for ZnO was 2.26×10^{-3} min^{-1} and 1.05×10^{-3} min^{-1}. The rate constant of ZnO/SnO$_2$ thin films in degrading MB and MO was found to be 7.36×10^{-3} min^{-1} and 1.81×10^{-3} min^{-1}, respectively. The recyclability of ZnO/SnO$_2$ thin films as a photocatalyst was carried out by performing the photodegradation of MB and MO for five cycles. The % photocatalytic degradation efficiency of ZnO/SnO$_2$ after five cycles is shown in Fig. 13c. The results show that the ZnO/SnO$_2$ films remain stable after five cycles of photodegradation of MB and MO.

The rate constants calculated for various photocatalysts showed that the degradation of MB is faster than MO. The absorbance spectra (Fig. 11g–i) for mixed dye (MO–MB) also confirm that MB degrades faster as compared with MO. This is due to the presence of the azo group in MO, which makes it more stable, hence delaying the degradation rate as compared with MB [34]. Moreover, the negatively charged photocatalyst (n-type) increases the electrostatic attraction with cationic MB because of their opposite charge polarity. This leads to the easy adsorption of cationic MB on the film surface as compared with anionic MO. As a result, the degradation of MB is faster in comparison with MO.

The improved photocatalytic performance of ZnO/SnO$_2$ can be understood from the energy band diagram shown in Fig. 14. The band edge location of the conduction band (CB) and valence band (VB) of the semiconductor was

calculated by using the following equations:

$$E_{CB} = \chi - E_e - 0.5E_g, \tag{3}$$

$$E_{VB} = E_g - E_{CB}, \tag{4}$$

where χ is the absolute electronegativity of the semiconductor ($\chi = 5.79$ eV for ZnO and $\chi = 6.25$ eV for SnO$_2$ [35]), E_e is the energy of free electron on the hydrogen scale ($E_e \sim 4.5$ eV) and E_g is the band gap of the semiconductor. The position of CB edges of SnO$_2$ and ZnO versus normal hydrogen electrode was calculated by using Eq. (3). The $E_{CB}^{SnO_2}$ and E_{CB}^{ZnO} for SnO$_2$ and ZnO was found to be -0.15 eV and -0.39 eV, respectively. Similarly, the position of VB edge, i.e., $E_{VB}^{SnO_2}$ and E_{VB}^{ZnO} calculated by using Eq. (4) for SnO$_2$ and ZnO was found to be $+3.65$ eV and $+2.98$ eV, respectively. Since the CB edge of ZnO is more negative and its VB edge is less positive than SnO$_2$, ZnO/SnO$_2$ forms type-II heterostructure [36]. According to type II band alignment, when SnO$_2$ and ZnO form a heterostructure, the electron transfer occurs from ZnO to SnO$_2$ and the hole from SnO$_2$ to ZnO until a stable equilibrium is attained by the system (Eq. 5). This leads in the effective separation of electron and hole pairs. The holes are trapped by hydroxyl group (OH$^-$) or physisorbed water molecules at the ZnO surface to produce a hydroxyl radicals (OH*) and the electrons are captured by dissolved O$_2$ to generate superoxide anions (O$_2^{*-}$) as shown in Eqs. (6) and (7), respectively. Further, the hydroxyl radicals (OH*) and superoxide ions (O$_2^{*-}$) are particularly reactive to decompose organic pollutants present on the surface of the films because of their strong oxidizing and
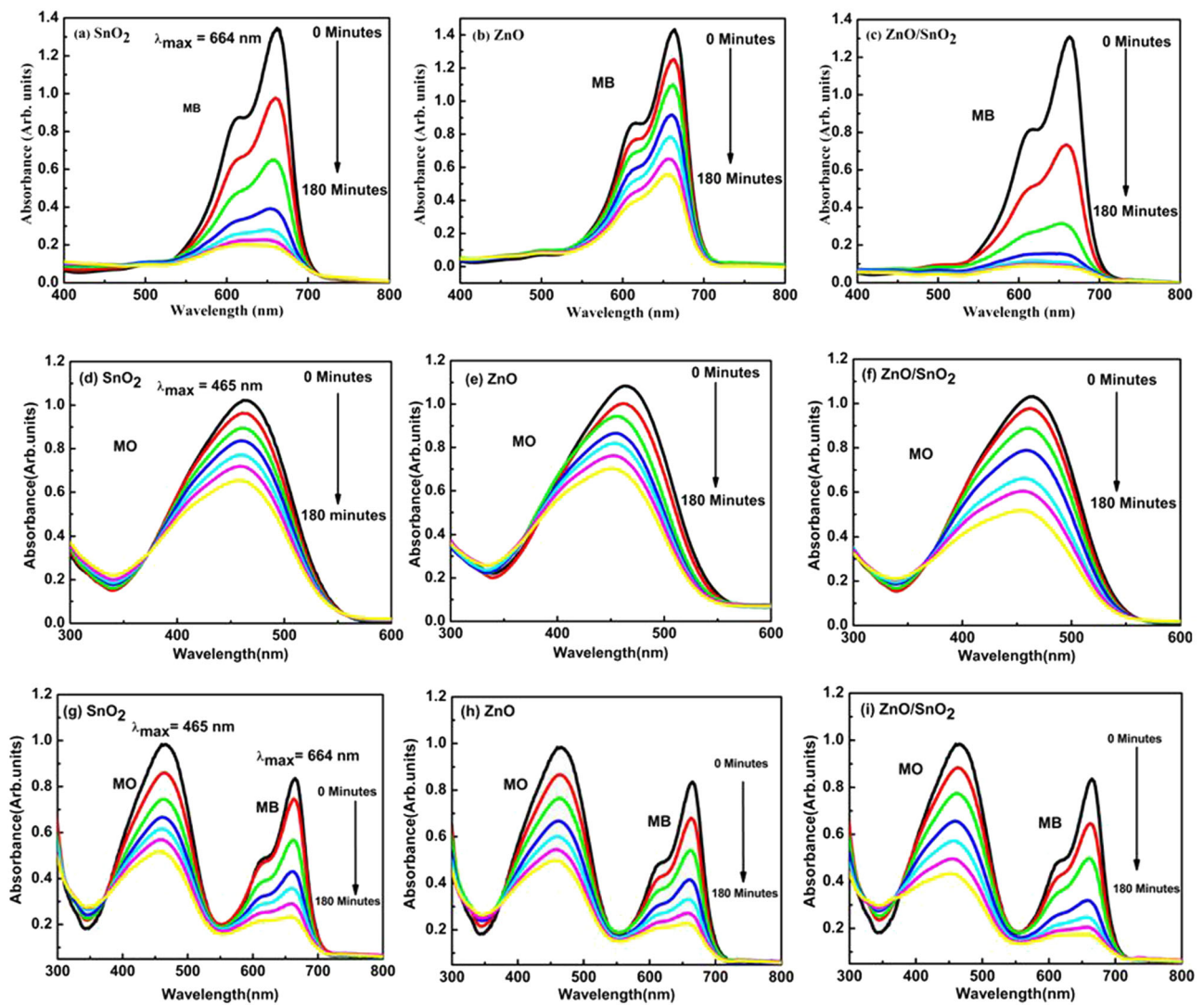
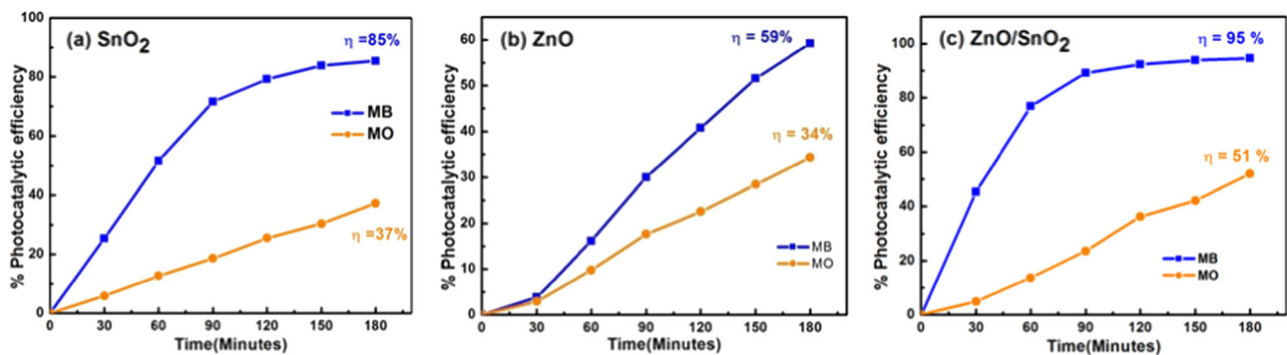Fig. 11 Absorbance spectra of degradation MB (a–c), MO (d–f), and MO–MB (g–i) by SnO_2, ZnO, and ZnO/SnO_2 thin films

Fig. 12 % Photocatalytic efficiency of a SnO_2, b ZnO, and c ZnO/SnO_2 thin films
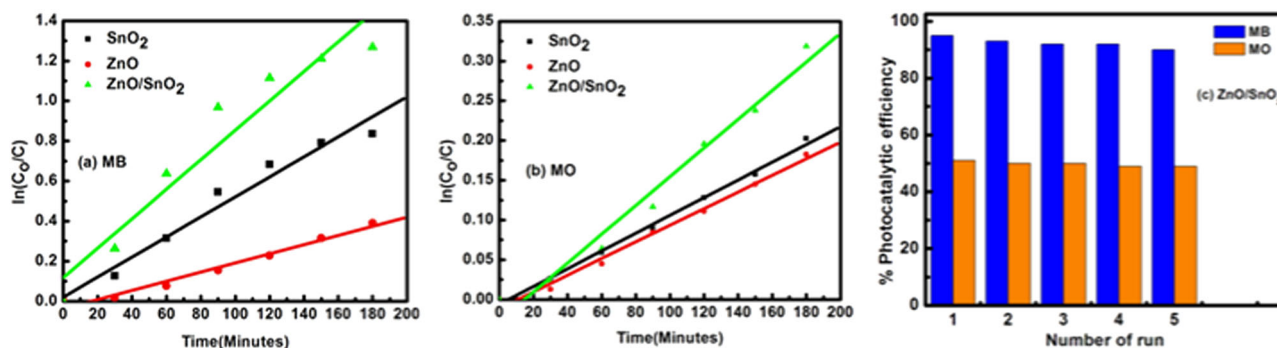
Fig. 13 Kinetics of photodegradation of **a** MB and **b** MO by SnO₂, ZnO, and ZnO/SnO₂ thin films, and **c** recyclability of ZnO/SnO₂ heterostructure in photodegradation of MB and MO
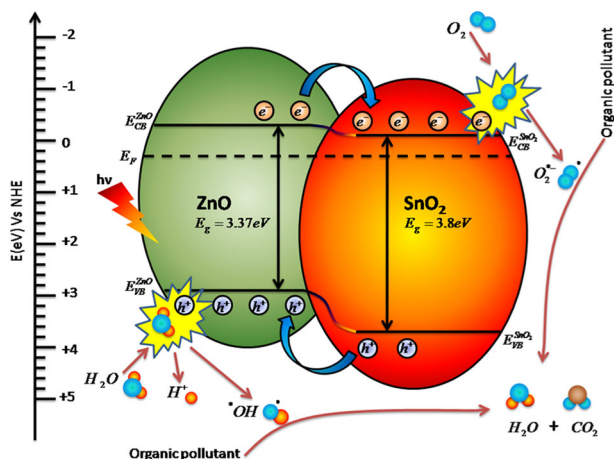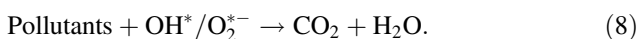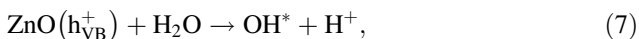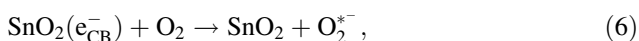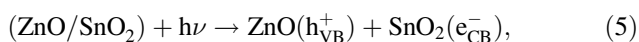

Fig. 14 Energy band diagram showing the charge-transfer process in the ZnO/SnO₂ heterojunction

reducing ability (Eq. 8). Thus, the effective separation of charge carrier is responsible for the higher photocatalytic activity of the ZnO/SnO₂ films as compared with the monocomponent thin films. The possible reaction for the photocatalytic activity of ZnO/SnO₂ catalyst is listed below

$$(ZnO/SnO_2) + h\nu \rightarrow ZnO(h_{VB}^+) + SnO_2(e_{CB}^-), \quad (5)$$

$$SnO_2(e_{CB}^-) + O_2 \rightarrow SnO_2 + O_2^{*-}, \quad (6)$$

$$ZnO(h_{VB}^+) + H_2O \rightarrow OH^* + H^+, \quad (7)$$

$$Pollutants + OH^*/O_2^{*-} \rightarrow CO_2 + H_2O. \quad (8)$$

4 Conclusion

This work presents the wettability and photocatalytic studies of SnO₂, ZnO, and ZnO/SnO₂ thin films deposited on glass substrate by sol–gel spin coating technique. The result shows that ZnO/SnO₂ thin films exhibited superhydrophilic character with a very high degree of transparency. The photocatalytic activity of the films was studied using model pollutants in a solid and liquid phase. It was shown that the efficiency of ZnO/SnO₂ thin films was superior in comparison to ZnO and SnO₂ thin films. This is attributed to the formation of heterostructure between ZnO and SnO₂, which suppresses the charge recombination. We believe a super-hydrophilic film with high transparency can have potential application in antifogging and self-cleaning.

Compliance with ethical standards

Conflict of interest The authors declare that they have no conflict of interest.

Publisher's note Springer Nature remains neutral with regard to jurisdictional claims in published maps and institutional affiliations.

References

1. Fujishima A, Zhang X (2006) Titanium dioxide photocatalysis: present situation and future approaches. Comptes Rendus Chimie 9:750–760.
2. Krishna MG, Madhurima V, Purkayastha DD (2013) Metal oxide thin films and nanostructures for self-cleaning applications: current status and future prospects. Eur Phys J Appl Phys 62:30001
3. Drelich J, Chibowski E, Meng DD, Terpilowski K (2011) Hydrophilic and superhydrophilic surfaces and materials. Soft Matter 7:9804–9828

4. Feng L, Li S, Li Y, Li H, Zhang L, Zhai J, Song Y, Liu B, Jiang L, Zou D (2002) Super-hydrophobic surfaces:From natural to artificial. Adv Matter 14:1857–1860

5. Feng X, Feng L, Jin M, Zhai J, Jiang L, Zhu D (2004) Reversible super-hydrophobicity to super-hydrophilicity transition of aligned ZnO nanorod films, photoinduced superhydrophilicity and photocatalytic properties of ZnO nanoplatelets. J Am Chem Soc 126:62–63

6. Okada K, Tokudome Y, Falcaro P, Takamatsu Y, Nakahira A, Takahashi M (2012) Titanate nanofunnel brushes: toward functional interfacial applications. Chem Commun 48:6130–6132

7. Barreca D, Gasparotto A, Maccato C, Tondello E, Stangar UL, Patil SR (2009) Photoinduced superhydrophilicity and photocatalytic properties of ZnO nanoplatelets. Surf Coat Tech 203:2041–2045

8. Papadopoulou EL, Barberoglou M, Zorba V, Manousaki A, Pagkozidis A, Stratakis E, Fotakis C (2009) Reversible photoinduced wettability transition of hierarchical ZnO structures. J Phys Chem C 113:2891–2895

9. Langlet M, Permpoon S, Riassetto D, Berthome G, Pernot E, Joud JC (2006) Photocatalytic activity and photo-induced superhydrophilicity of sol–gel derived TiO$_2$ films. J Photoch Photobio A 181:203–214

10. Simonsen ME, Li Z, Sogaard EG (2009) Influence of the OH groups on the photocatalytic activity and photoinduced hydrophilicity of microwave assisted sol–gel TiO$_2$ film. Appl Surf Sci 255:8054–8062

11. Padmavathy N, Vijayaraghavan R (2008) Enhanced bioactivity of ZnO nanoparticles-an antimicrobial study. Sci Technol Adv Mater 9:035004

12. Wang C, Chu X, Wu M (2006) Detection of H$_2$S down to ppb levels at room temperature using sensors based on ZnO nanorods. Sens Actuat B-Chem 113:320–323

13. Moafi HF, Shojaie AF, Zanjanchi MA (2011) Photocatalytic self-cleaning properties of cellulosic fibers modified by nano-sized zinc oxide. Thin Solid Films 519:3641–3646

14. Behnajady MA, Modirshahla N, Hamzavi R (2006) Kinetic study on photocatalytic degradation of C.I. Acid Yellow 23 by ZnO photocatalyst. J Hazard Mater 133:226–232

15. Talinungsang, Purkayastha DD, Krishna MG (2018) Dopant controlled photoinduced hydrophilicity and photocatalytic activity of SnO$_2$ thin films. Appl Surf Sci 447:724–731

16. Liu Y, Koep E, Liu M (2005) A highly sensitive and fast-responding SnO$_2$ sensor fabricated by combustion chemical vapor deposition. Chem Mater 17:3997–4000

17. Wang W, Zhu Y, Yang L (2007) ZnO–SnO$_2$ hollow spheres and hierarchical nanosheets: hydrothermal preparation, formation mechanism. Adv Funct Mater 17:59–64

18. Cun W, Jincai Z, Xinming W, Bixian M, Guoying S, Pingan P, Jiamo F (2002) Preparation, characterization and photocatalytic activity of nano-sized ZnO/SnO$_2$ coupled photocatalysts. Appl Catal B-Environ 39:269–279

19. Wang C, Wang X, Xu B, Zhao J, Mai B, Peng P, Sheng G, Fu J (2004) Enhanced photocatalytic performance of nanosized coupled ZnO/SnO$_2$ photocatalysts for methyl orange degradation. J Photoch Photobio A-Chem 168:47–52

20. Zhang M, An T, Hu X, Wang C, Sheng G, Fu J (2004) Preparation and photocatalytic properties of a nanometer ZnO–SnO$_2$ coupled oxide. Appl Catal A 260:215–222

21. Modirshahla N, Hassani A, Behnajady MA, Rahbarfam R (2011) Effect of operational parameters on decolorization of Acid Yellow 23 from wastewater by UV irradiation using ZnO and ZnO/SnO$_2$ photocatalysts. Desalination 271:187–192

22. Hamrouni A, Lachheb H, Houas A (2013) Synthesis, characterization and photocatalytic activity of ZnO-SnO$_2$ nanocomposites. Mater Sci Eng B 178:1371–1379

23. Liu R, Huang Y, Xiao A, Liu H (2010) Preparation and photocatalytic property of mesoporous ZnO/SnO$_2$ composite Nanofibers. J Alloy Compd 503:103–110

24. Uddin Md, Nicolas Y, Olivier C, Toupance T, Servant L, Muller M, Kleebe H, Ziegler J, Jaegermann W (2012) Nanostructured SnO$_2$−ZnO heterojunction photocatalysts showing enhanced photocatalytic activity for the degradation of organic dyes. Inorg Chem 51:7764–7773

25. Lamba R, Umar A, Mehta SK, Kansal SK (2015) Well-crystalline porous ZnO–SnO$_2$ nanosheets: an effective visible-light driven photocatalyst and highly sensitive smart sensor material. Talanta 131:490–498

26. Upadhaya D, Talinungsang, Kumar P, Purkayastha DD (2019) Tuning the wettability and photocatalytic efficiency of heterostructure ZnO-SnO$_2$ composite films with annealing temperature. Mat Sci Semicon Proc 95:28–34

27. Zhou M, Yu J, Liu S, Zhai P, Jiang L (2008) Effects of calcination temperatures on photocatalytic activity of SnO$_2$/TiO$_2$ composite films prepared by an EPD method. J Hazard Mater 154:1141–1148

28. Kaneva N, Stambolova I, Blaskov V, Dimitriev Y, Vassilev S, Dushkin C (2010) Photocatalytic activity of nanostructured ZnO films prepared by two different methods for the photoinitiated decolorization of malachite green. J Alloy Compd 500:252–258

29. Wenzel RN (1936) Resistance of solid surfaces to wetting by water. Ind Eng Chem 28:988–994

30. Chen Y, Zhang Y, Shi L, Li J, Xin Y (2012) Transparent super-hydrophobic/superhydrophilic coatings for self-cleaning and anti-fogging. Appl Phys Lett 101:033701

31. Chen Y, Zhang C, Huang W, Yang C, Huang T, Situ Y, Huang H (2013) Synthesis of porous ZnO/TiO$_2$ thin films with super-hydrophilicity and photocatalytic activity via a template-free sol–gel method. Surf Coat Tech 258:531–538

32. Rezayi T, Entezari MH (2016) Wettability property varies with different morphologies of ZnO nanpoarticles deposited on glass and modified by stearic acid. New J Chem 40:2582–2591

33. Owens DK, Wendt RC (1969) Estimation of the surface free energy of polymers. J Appl Polym Sci 13:1741–1747

34. Enesca A, Isac L, Duta A (2013) Hybrid structure comprised of SnO$_2$, ZnO and Cu$_2$S thin film semiconductors with controlled optoelectric and photocatalytic properties. Thin Solid Films 542:31–37

35. Xu Y, Schoonen MAA (2000) The absolute energy positions of conduction and valence bands of selected semiconducting minerals. Am Mineral 85:543–556

36. Zhang L, Jaroniec M (2018) Toward designing semiconductor-semiconductor heterojunctions for photocatalytic applications. Appl Surf Sci 430:2–38